이학석사 학위논문

Seasonal and spatial variations of air–sea heat exchange in the seas around the Korean Peninsula: Based on the observations (I-ORS and ESROB) and reanalysis products (CFSv2 and MERRA-2) from 2011 to 2016

2011-2016년 한반도 주변 해역에서 해양-대기 열 교환의 계절적 및 공간적 변동

2019년 8월

서울대학교 대학원

지구환경과학부

여 다 은

Seasonal and spatial variations of air–sea heat exchange in the seas around the Korean Peninsula: Based on the observations (I-ORS and ESROB) and reanalysis products (CFSv2 and MERRA-2) from 2011 to 2016

지도 교수 남 성 현

이 논문을 이학석사 학위논문으로 제출함
2019년 8월

서울대학교 대학원
지구환경과학부
여 다 은

여다은의 이학석사 학위논문을 인준함
2019년 8월

위 원 장 조 양 기 (인)

부위원장 남 성 현 (인)

위 원 박 경 애 (인)

Abstract

It is important to understand the ocean–atmosphere heat exchange for a better understanding of the process and for predicting the weather and climate systems. In the seas around the Korean Peninsula (KP), the annual cycles of most oceanic and atmospheric variables have long been well recognized, whereas those of the ocean–atmosphere heat exchange are still not completely clear primarily owing to a lack of *in-situ* observations applied to estimate the surface heat flux. This is particularly true over the region affected by the Tsushima Warm Current (TWC), where cold and dry air and a northwesterly wind over the warm sea surface enhance the heat exchange during the winter monsoons (when the ocean loses heat), which may often be over or underestimated through reanalysis model products. Herein, we present estimates of the mean annual cycles of air–sea heat fluxes from *in-situ* observations at two locations (I-ORS and ESROB) and using two reanalysis products (CFSv2 and MERRA-2) during the period of 2011 to 2016. The results show that the net heat loss of the ocean (net heat flux (NHF) of −68 W m^{-2}, positive downward) at ESROB near the east coast of Korea is 146 W m^{-2} larger than that (+78 W m^{-2}, e.g., net heat gain) at I-ORS, which is located ~250 km southwest of KP, except in June when the incoming shortwave radiation flux (SWR) decreases significantly (by 208 W m^{-2}) only at the I-ORS, which is associated with the Meiyu-Baiu rainband. More sensible and latent heat losses (SHF and LHF) of 32 and 47 W m^{-2} during both winter and spring, respectively, and less LHF by 22 W m^{-2} during fall,

were observed at ESROB than at I-ORS. The CFSv2 yields −24, −84, −41, and −180 W m^{-2} (−43, −110, −56, and −120 W m^{-2}) in terms of the average NHF, winter SHF, and spring and fall LHFs at I-ORS (ESROB), whereas MERRA-2 yields −28, −56, −26, and −161 W m^{-2} (−108, −134, −71, and −155 W m^{-2}), which is indicative of significant biases in the air–sea temperature difference and the wind speed. Spatial distributions of SHF and LHF of both reanalysis products, which are consistent each other as well as with the observations despite their biases, indicate the significant impact of TWC and the associated currents through the sea surface temperature and saturation-specific humidity on the annual cycles of the ocean–atmosphere heat exchange within the region.

Keyword : Ieodo Ocean Research Station (I-ORS), East Sea Real-time Ocean Buoy (ESROB), Air-sea heat exchange, Seasonal variation, Tsushima Warm Current, Cheju Warm Current, Chinese Coastal Current, East Korea Warm Current, North Korea Cold Current

Student Number : 2017-29237

Table of Contents

List of Tables

List of Figures

Chapter 1. Introduction

An air–sea heat exchange occurs at the sea surface in the forms of radiation and turbulence, depending on the internal characteristics of the ocean and the atmospheric conditions. It is important to understand the ocean–atmosphere heat exchange for a better understanding of the process and for predicting the weather and climate systems (Webster and Lukas 1992; Fairall et al. 1996a; Qui et al. 2004; Small et al. 2008; Kim et al. 2016). In particular, it is known that a large amount of heat is transferred from the ocean into the atmosphere and vice versa in regions of strong oceanic and/or atmospheric variability, i.e., regions affected by the Kuroshio Current and the Tsushima Warm Current (TWC), where oceanic variability associated with a meandering of the currents and eddies, along with atmospheric variability associated with the East Asian monsoons, are significant (Na et al. 1999; Hirose et al. 1996; Hirose et al. 1999; Kim and Kwon 2003; Chu et al. 2005; Yu and Weller 2007; Small et al. 2008; Liu et al. 2014; Seo et al. 2014; Kwak et al. 2015; Kim et al. 2016). Fronts and eddies in these regions affect the atmosphere with changes in the near-surface stability, surface stress, height of the boundary layer, and atmospheric pressure, thereby yielding variations in the surface heat fluxes (Small et al. 2008).

There have been several studies showing the effects of the East Asian monsoons and TWC on the ocean–atmosphere heat exchange in the seas

around the Korean Peninsula (KP). The net heat fluxes (NHF) in the region have been estimated from weather maps dating back from 1978 to 1995 (Na et al. 1999), and from the Comprehensive Ocean-Atmosphere Data Set from 1960 to 1990 (Hirose et al. 1996; Hirose et al. 1999) and from 1945 to 1989 (Chu et al. 2005). These studies showed the distinct annual variation of the surface heat flux through which the ocean gains (loses) heat from the atmosphere during summer (winter) owing to the TWC with warm and moist (cold and dry) winds associated with the summer (winter) monsoons, respectively. Despite the long and similar periods, spanning from the 1960s to 1990s, considered in previous studies, the estimated heat fluxes in the seas around the KP with no or few *in-situ* observations are inconsistent among the such studies, showing significant differences of ~70 $\mathrm{W\ m^{-2}}$ for shortwave radiation (SWR) fluxes in July, ~60 $\mathrm{W\ m^{-2}}$ for sensible heat fluxes (SHF) in January, and ~100 $\mathrm{W\ m^{-2}}$ for latent heat fluxes (LHF) in January. Annual variations of the surface heat flux have been reported from *in-situ* observations using surface ocean buoys (Park et al. 2003; Subrahamanyam et al. 2007), yet only turbulent heat fluxes, rather than the NHF, are available. With rare long and continuous time-series observations on both atmospheric and oceanic parameters, most previous studies have utilized reanalysis data (Liu et al. 2014; Sim et al. 2018) or only short *in-situ* observational data (Yun et al. 2015), which cannot provide information on robust seasonal variations (annual cycles), or the effects of ocean circulation with TWC branches such as the Cheju Warm Current (CWC) and East Korea Warm Current (EKWC) on the NHF and its components.

Thus, this study aims to address the annual cycles of the spatial

variability of air–sea heat fluxes in the seas around the KP using a long time-series of observational and high-resolution reanalysis data. In particular, we used time-series data collected at two observational sites in the region, name, the Ieodo Ocean Research Station (I-ORS) and the East Sea Real-time Ocean Buoy (ESROB), where both atmospheric and oceanic parameters have been simultaneously measured for years (Fig. 1). The I-ORS is within the vicinity of the main path or western wall of the TWC, whereas ESROB near the Korean east coast is within the vicinity of main path or western wall of the EKWC. These two sites are suitable for examining the influences of both the TWC and Asian monsoons on the annual cycles of the NHF and its components. The measurements, data, and methods used in this study are described in section 2. The results on the seasonal and spatial heat flux variations are provided in section 3. The results are discussed in section 4. Finally, the materials are summarized and some concluding remarks are given in section 5.

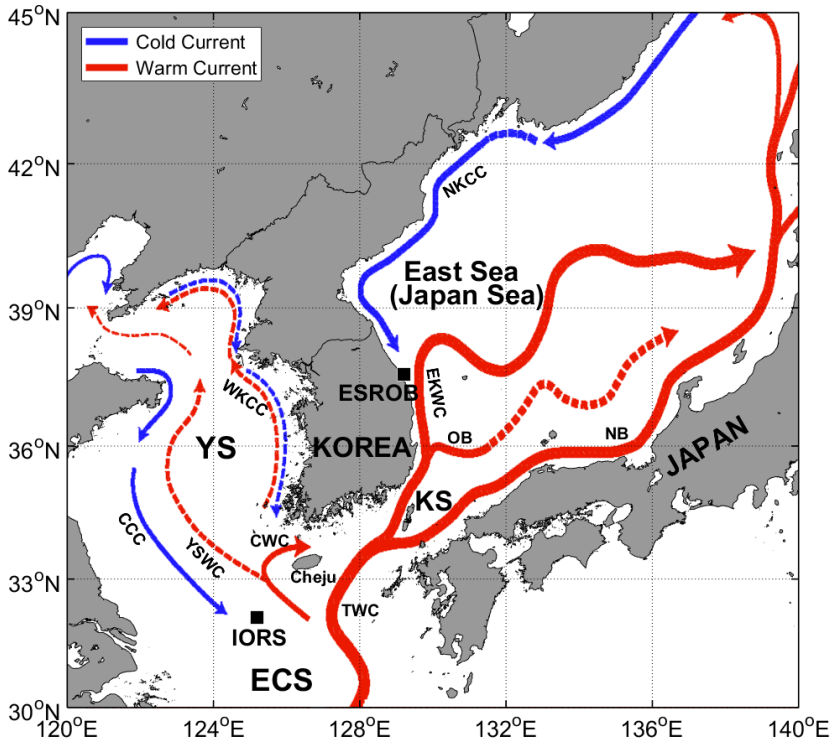

Figure 1. Station map with locations of I-ORS and ESROB and regional surface circulation in the Yellow Sea (YS), East China Sea (ECS), and East Sea (Japan Sea) around the Korean Peninsula, based on Park et al. (2013). Here, warm and cold currents are shown with red and blue colors: CCC, Chinese Coastal Current; YSWC, Yellow Sea Warm Current; WKCC, West Korea Coastal Current; CWC, Cheju Warm Current; TWC, Tsushima Warm Current; EKWC, East Korea Warm Current; OB, Offshore branch of TWC; NB, Nearshore branch of TWC; and NKCC, North Korea Cold Current.

Chapter 2. Data & Methods

Long (> 4 years) time-series data collected at the two observational sites, namely, I-ORS and ESROB, were used in this study. The I-ORS is a multi-purpose marine platform, located ~149 km southwest of Cheju Island at 32.123°N, 125.182°E (water depth of ~41 m) where the atmospheric pressure (P), air temperature (T_{air}), relative humidity, downward shortwave radiation (ISW), wind speed (U), and water temperature have been measured since June 2003 (Shim et al. 2004) (Table 1, Fig. 1). The main deck height of the tower is 33.5 m, and the sensors attached to the main deck are listed in Table 1. The same parameters and downward longwave radiation (ILW) have been measured at the surface mooring ESROB (37.573°N, 129.215°E), located ~8 km from the Korean east coast (water depth of ~130 m) (Fig. 1). Specifications of the conductivity-temperature-depth sensor, pyranometer, pyrgeometer, barometer, thermo-hygrometer, and wind sensor attached to the surface buoy and mooring line are listed in Table 1. The developments of the ESROB, including the technical improvements, are detailed in Nam et al. (2005) and Park et al. (2018). The observational data simultaneously collected with a time interval of 10 min at the two sites from November 2011 to July 2016 were used here. At the I-ORS, ILW was not measured during this period, whereas ISW was observed and processed to remove the abnormal values, where the outliers exceed 3 standard deviations from the mean time (Lee et al. 2017).

Table 1. List of parameters and heights of measurements, sensor types, and models with their specifications, and the period of operation and data used in this study at the I-ORS and ESROB.

Sites	Parameters of measurements	Heights of measurements	Sensor types (Model/Spec.)	Operation period	Period of data used in this study
I-ORS	Downward shortwave radiation (ISW)	35 m	Pyranometer (MS-802, EKO)	Since 2003	2011.11~2016.07
	Downward longwave radiation (ILW)	Not available			
	Atmospheric pressure (P)	35 m	Barometer (PTB210B, VAISALA)	Since 2003	2011.11~2016.07
	Air temperature (T_{air}) and relative humidity (1)	36.6 m	Thermo-hygrometer (HMP155, VAISALA)	Since 2003	2011.11~2011.12, 2013.01~2016.07
	Air temperature (T_{air}) and relative humidity (2)	41.5 m	Thermo-hygrometer (HMP155, VAISALA)	Since 2003	2012.01~2012.12
	Wind speed (U)	42.3 m	Anemometer (05106 wind monitor, R. M. YOUNG)	Since 2003	2011.11~2016.07
	Water temperature	5 m	CT (CT3919, Aanderaa)	Since 2003	2011.11~2016.07
ESROB	Downward shortwave radiation (ISW)	3.4 m	Pyranometer (PSP, EPLAB)	Since 2011	2011.11~2016.07
	Downward longwave radiation (ILW)	3.4 m	Pyrgeometer (PIR, EPLAB)	Since 2011	Not used
	Atmospheric pressure (P)	1 m	Barometer (PTB210, VAISALA)	Since 2000	2011.11~2016.07
	Air temperature (T_{air}) and relative humidity	3.3 m	Thermo-hygrometer (HMP155, VAISALA)	Since 2000	2011.11~2016.07
	Wind speed (U)	3.4 m	Anemometer (05106 wind monitor, R. M. YOUNG)	Since 1999	2011.11~2016.07
	Water temperature	5 m	CTD (SBE37IM, SBE)	Since 2000	2011.11~2016.07

Two reanalysis datasets, Climate Forecast System version 2 (CFSv2) and Modern-Era Retrospective analysis for Research and Applications version 2 (MERRA-2), for the same period as the observational data were used in this study (Jin and Yu 2013). Both reanalysis products provide data on the surface heat fluxes and various parameters including the ISW, ILW, SHF, LHF, precipitation rate, P, T_{air}, specific humidity (q_{air}), water temperature (T_{sea}) (CFSv2, temperature at 5 m; MERRA-2, sea surface temperature or SST), and U used here. The retrospective CFSv2 forecast and MERRA-2 reanalysis data were produced with time intervals of 6 and 1 h, and zonal and meridional resolutions of 0.2° for the atmosphere model and 0.5° for the ocean model (Saha et al. 2014), with 1/2° × 2/3° (Gelaro et al. 2017), respectively (Table 2). In addition, the gridded satellite altimeter data were used to identify the seasonal and spatial variations of the ocean surface current in the region, which were produced daily with spatial resolution of 0.25º X 0.25 º for the same period.

Table 2. Spatial and temporal coverage and resolutions of CFSv2 and MERRA-2 used in this study.

Reanalysis data	**Spatial resolution [lat. ✕ lon.]**	**Meridional coverage (used in this study)**	**Zonal coverage (used in this study)**	**Time interval**	**Period (used in this study)**
CFSv2	0.2° ✕ 0.2°	90°S~90°N (30°N~45°N)	0°E~360°E (120°E~140°E)	6 hrs	March 2011 to present (2011.11~2016.07)
CFSv2 (sea temp.)	0.5° ✕ 0.5°	90°S~90°N (30°N~45°N)	0°E~360°E (120°E~140°E)	6 hrs	March 2011 to present (2011.11~2016.07)
MERRA-2	0.5° ✕ 0.67°	90°S~90°N (30°N~45°N)	0°E~180°E (120°E~140°E)	1 hr	1980 to present (2011.11~2016.07)

The observed heat fluxes were calculated using the bulk formula following Fairall et al. (1996a) and Smith et al. (1996), where the NHF is the sum of the SWR, the longwave radiation flux (LWR), SHF, and LHF:

$$\mathrm{NHF} = \mathrm{SWR} - \mathrm{LWR} - \mathrm{SHF} - \mathrm{LHF} \quad (1)$$

$$\mathrm{SWR} = (1 - \alpha)ISW \quad (1a)$$

$$\mathrm{LWR} = \varepsilon(\sigma {T_{sea}}^4 - ILW) \quad (1b)$$

$$\mathrm{SHF} = \rho \mathrm{C_P} \mathrm{C_h} U(T_{sea} - T_{air}) \quad (1c)$$

$$\mathrm{LHF} = \rho \mathrm{L_e} \mathrm{C_e} U(q_{sea} - q_{air}) \quad (1d)$$

where α (=0.055), ε (=0.97), and σ are the albedo, emissivity, and Stefan–Boltzmann constant, and 5.67×10^{-8} W $\mathrm{m^{-2}}$ $\mathrm{K^{-4}}$, respectively. Here, Eqs. (1), (1a), (1c), and (1d) were applied to the observational data (LWRs were replaced with an LWR of CFSv2), and Eqs. (1), (1a), (1b) were applied to the two reanalysis data. The observed SHF and LHF were estimated using the Coupled Ocean–Atmosphere Response Experiment version 3.0 (COARE 3.0) algorithm (Fairall et al. 1996a; Fairall et al. 2003). In Eq. (1c)–(1d), ρ, $\mathrm{C_P}$ (=1004.67 J $\mathrm{kg^{-1}}$ $\mathrm{K^{-1}}$), $\mathrm{L_e}$, $\mathrm{C_h}$, $\mathrm{C_e}$, and q_{sea} denote the air density, specific heat capacity of air, latent heat of evaporation, transfer coefficients for sensible and latent heats, and saturation-specific humidity, respectively. The observed variables (P, T_{air}, q_{air}, U, ISW, ILW, and their measurement heights, water temperature, and measurement depth, latitude, and longitude) were used for the COARE 3.0 algorithm to estimate SHF and LHF where the warm layer and cool skin effects were applied (Fairall et al. 1996b; Ward 2006; Kawai and Wada 2007). In the COARE 3.0 algorithm, the

transfer coefficients were obtained considering the roughness lengths and vertical profiles of T_{air} and q_{air} (Fairall et al. 1996a). The value of q_{air} was calculated by converting the observed relative humidity with P and T_{air}, following Murphy and Koop (2005), and following the COARE 3.0 algorithm, q_{sea} is calculated from P and T_{sea} for both observational and reanalysis data.

Chapter 3. Results

3.1 Seasonal variations of heat fluxes at I-ORS and ESROB: Observations

The NHF at the I-ORS shows clear seasonal variations with positive (downward or ocean gain heat from the atmosphere) from March to October (MAMJJASO) and negative fluxes in the remaining months (Fig. 2a). The annual mean of the NHF is approximately 89 W m^{-2} (net heat gain), and the positive and negative mean values are 202 and −139 W m^{-2}, respectively. The positive NHF is dominated by the SWR, whereas the negative NHF is dominated by the fluxes. In particular, the annual mean of the SWR is 234 W m^{-2} with a larger flux during the warm season (MAMJJASO) and a sharp decrease in June of ~90 W m^{-2}. The negative LWR, SHF, and LHF are enhanced during the winter, yielding annual mean values of −55, −18, and −83 W m^{-2}, respectively.

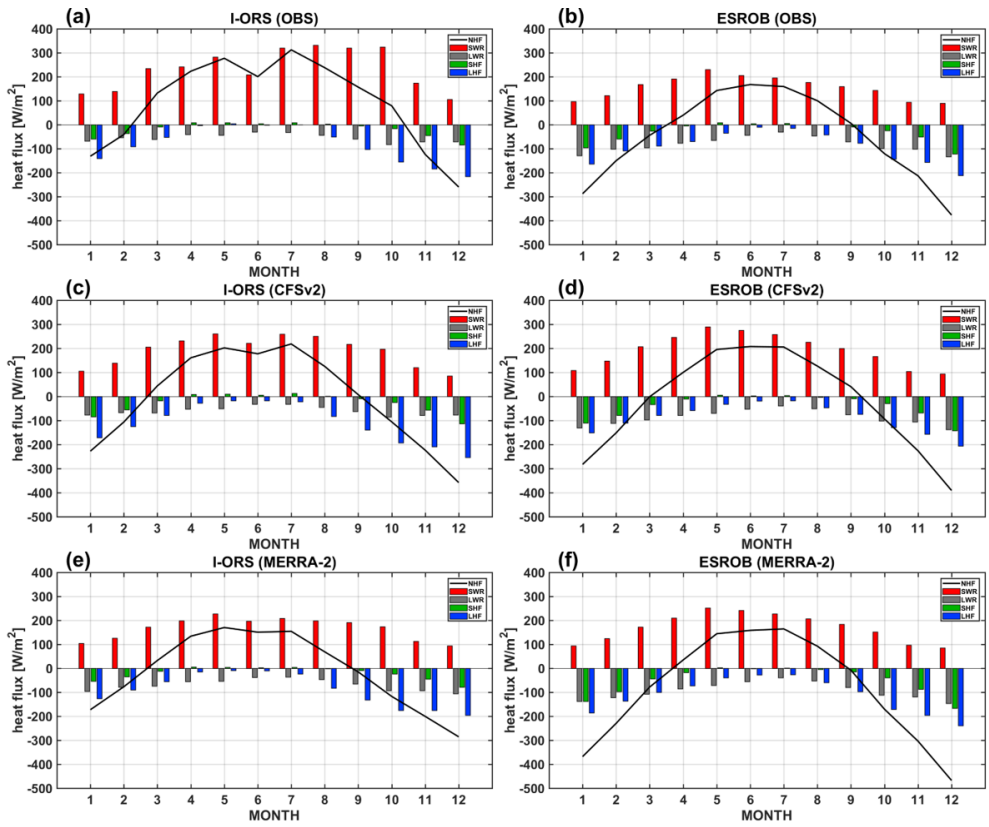

Figure 2. Annual climatology of heat fluxes (SWR, red; LWR, gray; SHF, green; LHF, blue; and NHF, black) at I-ORS (left) and ESROB (right). (a, b) Observation, (c, d) CFSv2, and (e, f) MERRA-2 at (a, c, e) I-ORS and (b, d, f) ESROB.

The NHF at the ESROB shows a similar but slightly decreased (negatively shifted) seasonal variation with positive fluxes from April to September (AMJJAS) and negative fluxes in the remaining months (Fig. 2b). The annual mean of NHF is approximately $-32\ \mathrm{W\ m^{-2}}$ (net heat loss), and the positive and negative mean values are 124 and $-189\ \mathrm{W\ m^{-2}}$, respectively. Similarly, the positive NHF is dominated by the SWR (annual mean of 156 $\mathrm{W\ m^{-2}}$) whereas the negative NHF is dominated by the other fluxes (annual means of −67, −31, and $-93\ \mathrm{W\ m^{-2}}$, respectively). Note that the SWR at the ESROB does not show a decreasing pattern in June as shown in the I-ORS, but does show a positive peak in May (230 $\mathrm{W\ m^{-2}}$).

Despite the somewhat similar seasonal variations of LWR, SHF, and LHF between the two sites, e.g., negatively enhanced in the winter, the difference in heat flux between the I-ORS and ESROB shows a distinct seasonal pattern with significantly smaller annual mean values of the NHF and SWR at the ESROB than those at the I-ORS by 121 and 80 $\mathrm{W\ m^{-2}}$, respectively (the ocean gains less heat at the ESROB) (Fig. 3a). The difference in the NHF is positive in all seasons and is dominated by the difference in the SWR in the warm season except for June when the difference becomes negligible, which is associated with the drop in I-ORS in June. The difference in the SHF is also positive in all seasons and enhanced (~30 $\mathrm{W\ m^{-2}}$) in the winter (DJF), whereas the LHF difference is positively (~50 $\mathrm{W\ m^{-2}}$) and negatively ($\sim -20\ \mathrm{W\ m^{-2}}$) enhanced in spring and fall, which is indicative of more heat loss of the ocean at the ESROB by the SHF in the winter, and the LHF in the spring, whereas more heat gain occurs by the LHF in the fall.

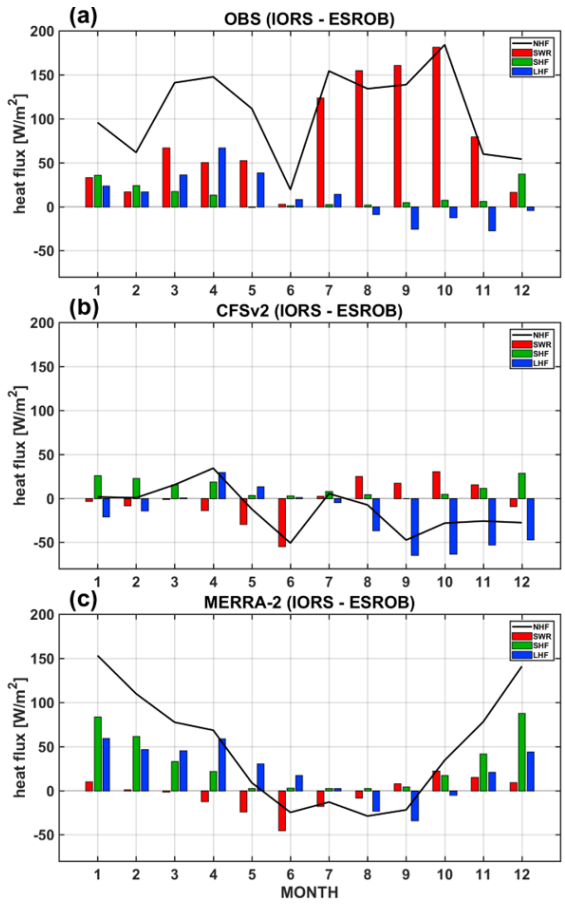

Figure 3. Difference in annual climatology for heat fluxes (SWR, SHF, LHF, and NHF) between I-ORS and ESROB from (a) the observations, (b) CFSv2, and (c) MERRA-2. Here, NHF is the sum of the SWR, SHF, and LHF, ignoring only the LWR.

3.2 Seasonal variation of heat fluxes at I-ORS and ESROB: Reanalysis products

Although both CFSv2 and MERRA-2 underestimate the downward NHF by an annual average of ~100 $W\ m^{-2}$ at the I-ORS, their consistent seasonal variations with observations are explained based on high correlation coefficients (Figs. 2a, 2c, and 2e, and Table 3). The correlation coefficients between the reanalyzed and observed NHF, SWR, SHF, and LHF are 0.96, 0.83, 0.98, and 0.98 for CFSv2, and 0.93, 0.78, 0.98, and 0.96 for MERRA-2, at the I-ORS. Despite a significant underestimation of the SWR by an annual average of ~55 $W\ m^{-2}$, the decrease in SWR observed at the I-ORS in June was consistently found from both reanalysis data (Figs. 2a, 2c, and 2e). The reanalysis products commonly underestimate the enhanced SWR in the warm season and overestimate the amplitudes of the negatively enhanced SHF and LHF in the winter, yielding negative differences in NHF over all seasons at the I-ORS (shaded parts in Table 3). The MERRA-2 overestimates the positive SWR for all months except December and underestimates the amplitude of negative the SHF and LHF in winter months (NDJF) more significantly than CFSv2 at I-ORS (Figs. 2a, 2c, and 2e, and Table 3).

Table 3. Difference between the reanalyzed and observed SWR, SHF, LHF, and NHF at the I-ORS, including the mean and standard deviation. A negative value (shaded) indicates an underestimation of the positive (downward) heat flux from the reanalysis data.

Term	Product	1	2	3	4	5	6	7	8	9	10	11	12	Mean	Std.
SWR	**CFSv2**	-24	1	-29	-10	-22	13	-60	-81	-103	-127	-54	-21	-43	43
	MERRA-2	-26	-13	-64	-44	-55	-12	-111	-133	-129	-150	-61	-12	-67	51
SHF	**CFSv2**	-26	-19	-9	0	1	2	4	0	-5	-8	-12	-29	-8	11
	MERRA-2	5	1	-3	-3	-4	-2	-4	-4	-5	-6	0	5	-2	4
LHF	**CFSv2**	-31	-33	-26	-25	-22	-17	-21	-32	-37	-37	-25	-37	-28	7
	MERRA-2	14	2	-3	-11	-13	-9	-23	-31	-29	-21	8	21	-8	17
NHF	**CFSv2**	-96	-65	-88	-62	-75	-23	-94	-113	-149	-185	-99	-98	-96	41
	MERRA-2	-41	-36	-100	-89	-107	-50	-158	-169	-172	-196	-77	-26	-102	59

Table 4. Same as Table 3 but for the ESROB.

Term	Product	1	2	3	4	5	6	7	8	9	10	11	12	Mean	Std.
SWR	**CFSv2**	13	26	39	54	60	70	61	49	40	24	10	5	38	22
	MERRA-2	-3	3	5	19	22	36	31	31	24	9	3	-4	15	14
SHF	**CFSv2**	-15	-18	-7	-5	-3	0	-2	-2	0	-6	-17	-21	-8	8
	MERRA-2	-43	-36	-19	-12	-7	-4	-4	-4	-5	-16	-36	-45	-19	16
LHF	**CFSv2**	14	-2	10	13	3	-9	-2	-4	2	14	0	6	4	8
	MERRA-2	-22	-28	-12	-3	-5	-18	-11	-17	-21	-28	-40	-28	-19	11
NHF	**CFSv2**	6	-2	43	60	53	40	46	26	35	27	-13	-14	26	26
	MERRA-2	-80	-80	-34	-5	2	-9	5	-8	-14	-50	-91	-91	-38	38

The correlation coefficients between the reanalyzed and observed NHF, SWR, SHF, and LHF data are 0.99, 0.98, 0.98, and 0.98 for CFSv2 and 0.99, 0.97, 0.98, and 0.97 for MERRA-2 at the ESROB (Figs. 2b, 2d, and 2f). The positive NHF (~124 $W\ m^{-2}$) during the warm season (from April to September) and the positive peak of SWR (~230 $W\ m^{-2}$) in May observed at the ESROB are consistently found from the two reanalysis products (positive NHF during the warm season of ~146 and ~98 $W\ m^{-2}$, and a peak of the SWR in May of ~290 and ~252 $W\ m^{-2}$ for CFSv2 and MERRA-2, respectively). Seasonal variations between the reanalyzed and observed turbulent fluxes (SHF and LHF) are consistent, commonly showing negative peaks of SHF (−121, −142, and −166 $W\ m^{-2}$ for the observation, CFSv2, and MERRA-2, respectively) and LHF (−212, −206, and −239 $W\ m^{-2}$) in December, and decreasing tends from January (SHF of −124 $W\ m^{-2}$ and LHF of −168 $W\ m^{-2}$ on average for two model data) to June (SHF of 0 $W\ m^{-2}$ and LHF of −24 $W\ m^{-2}$) and increasing trends from July (SHF of 3 $W\ m^{-2}$ and LHF of −22 $W\ m^{-2}$) to November (SHF of −78 $W\ m^{-2}$ and LHF of −176 $W\ m^{-2}$).

The overestimations of the SWR (by 3 to 70 $W\ m^{-2}$) and the amplitude of the negative SHF (by 2 to 45 $W\ m^{-2}$) of both reanalysis products are clear at the ESROB, yielding positive and negative NHF differences (Table 4). Here, CFSv2 overestimates, and MERRA-2 underestimates, the LHF by 4 and 19 $W\ m^{-2}$ on average annually, respectively. In addition, CFSv2 mostly underestimates (overestimates) the NHF by ~10 $W\ m^{-2}$ (~40 $W\ m^{-2}$) in the cold (warm) season, whereas

MERRA-2 primarily underestimates the NHF in all seasons except between May and July by 5–91 $W\ m^{-2}$ (Table 4). Overall, the amplitude differences between the observed and reanalyzed NHFs at the ESROB are approximately 70 $W\ m^{-2}$ less than those at the I-ORS. The two reanalysis data underestimate the SWRs at the I-ORS and overestimate those at the ESROB by ~43–67 and ~15–38 $W\ m^{-2}$, respectively (Tables 3 and 4).

The resultant spatial differences in heat fluxes between the I-ORS and ESROB locations are far from the observed temporal structure (Fig. 3). The difference in the NHF between the I-ORS and ESROB is within ±50 $W\ m^{-2}$ for CFSv2 while exceeding 100 $W\ m^{-2}$ in winter for MERRA-2, which is indicative of a poor performance of the reanalysis products (Figs. 3b and 3c). Although the June SWR drop observed at the I-ORS only is reproduced by both reanalysis products, CFSv2 and MERRA-2 are negatively peaked by 55 and 45 $W\ m^{-2}$, respectively, which is inconsistent with the near-zero difference in the SWR observed in June (Figs. 3a–3c). Here, CFSv2 better reproduces the difference in the SHF than MERRA-2, yielding enhanced winter (DJF) fluxes more consistently with the observations, which is unlikely for the case of MERRA-2, where strong (~45 $W\ m^{-2}$) overestimations of the difference in the LHF and SHF in winter and the resulting difference in the NHF between the two locations occur (Figs. 2 and 3, and Tables 3 and 4). The differences in the LHF in winter of CFSv2 (JF) and MERRA-2 (ND) have an opposite sign from the observed difference in the LHF because the enhanced winter LHFs are poorly reproduced by the two reanalysis products (Tables 3 and 4). Nevertheless, the enhanced differences in the LHF during spring and fall (the ocean loses more latent heat at the

ESROB in spring by 47 W m^{-2} and less in the fall by −22 W m^{-2}) are consistently reproduced by the two reanalysis products with the maximum observed difference in the LHF (~36 W m^{-2}) occurring in March and the minimum (~−25 W m^{-2}) occurring in September (Fig. 3). Thus, the spatial distributions of the SWR in June, the SHF in winter, and the LHFs in both spring and fall from the two reanalysis products are further examined in the next section.

3.3 Seasonal and spatial heat flux variations

Both reanalysis products commonly and consistently show that the SWR decreases at the I-ORS (but not ESROB) in June as observed. Despite the overall positive bias of the CFSv2 compared to the MERRA-2 by 10–40 W m^{-2}, spatial patterns of the June decrease in the SWR are consistent between the two reanalysis products, demonstrating a severe decrease in the SWR (~210 W m^{-2}) in the area south of 33°N where the I-ORS is located (Fig. 4). These spatial patterns of the June SWR being lower than those in May and July explain the decreased difference in the SWR between I-ORS and ESROB observed in June (Figs. 2 and 3).

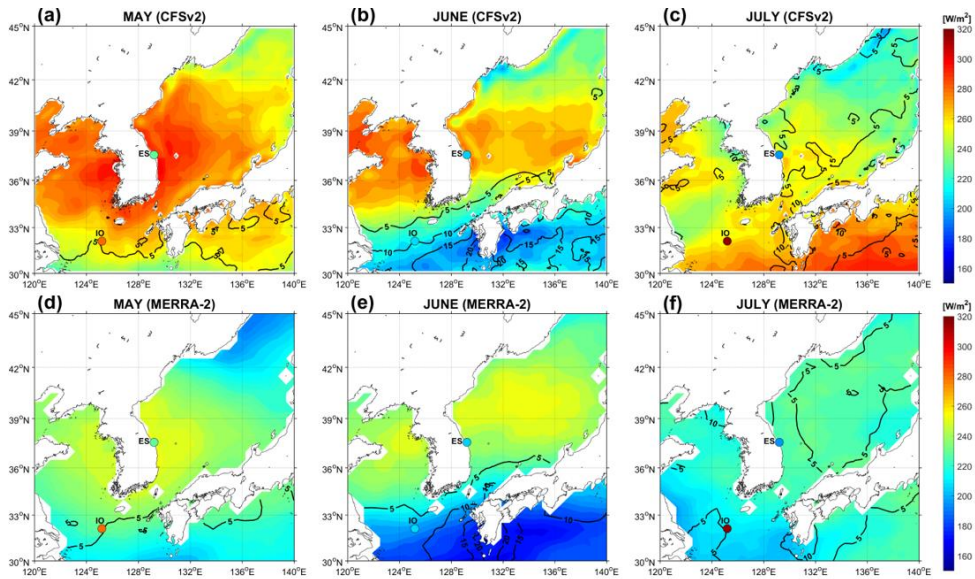

Figure 4. Spatial distribution of SWR (colors) in the seas around the Korean Peninsula in (a, d) May, (b, e) June, and (c, f) July from (a–c) CFSv2 and (d–f) MERRA-2. The rainfall in mm per day is indicated by the black contours. Here, the I-ORS and ESROB are labeled by IO and ES, respectively.

High winter (DJF) SHF losses observed at the I-ORS and ESROB were reproduced using the two reanalysis products (negatively enhanced to $-110\ \mathrm{W\ m^{-2}}$ in CFSv2 and $-90\ \mathrm{W\ m^{-2}}$ in MERRA-2), and the area of high SHF loss is closely linked to the TWC and its branches in the seas around the KP (Figs. 5a and 5b). The eastward and westward spreads of areas with low and high SHF losses in the southern and northern parts of the I-ORS match the paths of the Chinese Coastal Current (CCC) and Cheju Warm Current (CWC) (Figs. 1, 5a, and 5b). Because the I-ORS and ESROB are within the vicinity of the front between the CWC and CCC and between the EKWC and the North Korea Cold Current (NKCC), the winter SHF sharply varies within the vicinity of the two sites (Figs. 5a and 5b). The difference in air–sea temperature $(T_{sea} - T_{air})$, the most significant factor affecting the SHF based on a sensitivity test (see Appendix A), is enhanced along the paths of the TWC and its branches (CWC and EKWC), accounting for the enhanced SHF by warm water transported poleward from the northeastern ECS to the East Sea (high T_{sea} compared to T_{air}).

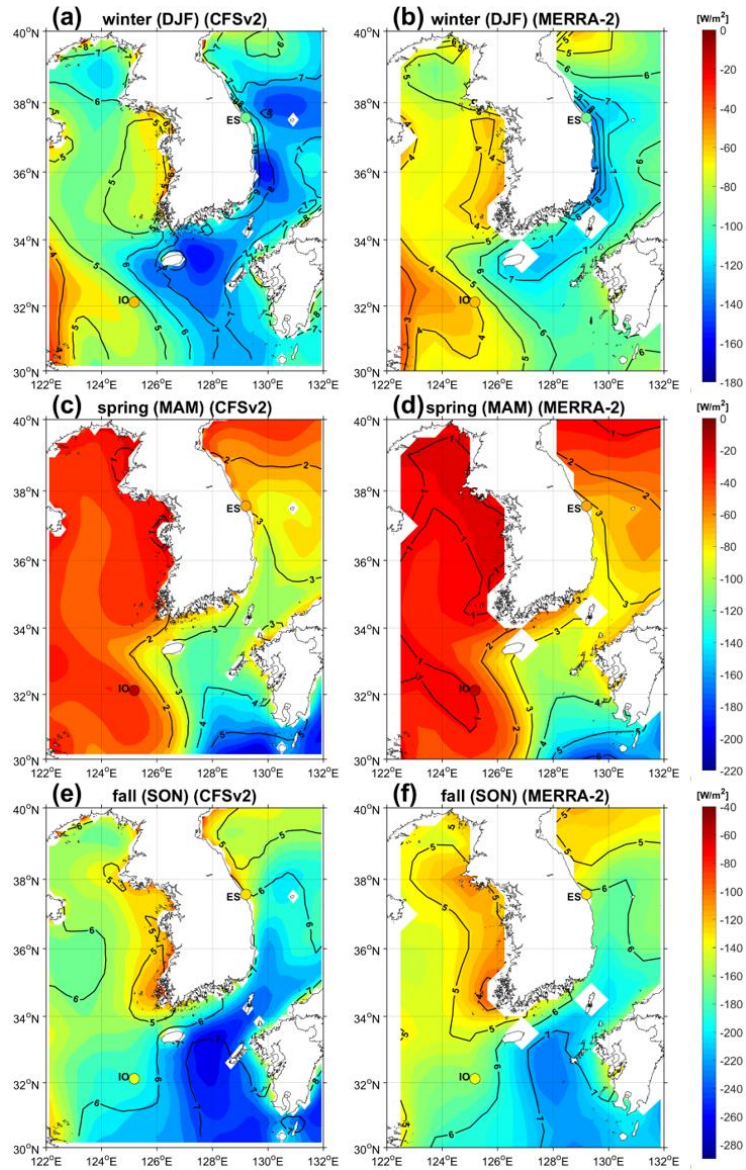

Figure 5. Spatial distribution of (a, b) winter (DJF) SHF, (c, d) spring (MAM) LHF, and (e, f) fall (SON) LHF from (a, c, e) CFSv2 and (b, d, f) MERRA-2 (indicated by color). The difference between sea surface temperature (SST) and 10-m air temperature in ºC and the difference between saturation specific humidity and 10-m air specific humidity in g kg^{-1} are shown through the contours in (a, b) and (c, d, e, and f), respectively.

Spatial patterns of LHF in spring (MAM) and fall (SON) also reflect the influences of the surface currents such as TWC, CWC, CCC, EKWC, and NKCC (Figs. 5c, 5d, 5e, and 5f). In spring, latent heat loss of the ocean through the LHF is the largest in the northeastern ECS and off the Korean east coast, particularly along the path of TWC, CWC, and EKWC (Figs. 5c and 5d). The higher LHF loss in spring (negatively enhanced) at the ESROB than at the I-ORS is explained by these patterns, where the EKWC reaches the ESROB and CCC, rather than TWC dominating the I-ORS (Figs. 3a, 5c, and 5d). The difference in air–sea humidity $(q_{sea} - q_{air})$, the most significant factor affecting the LHF based on the sensitivity test (see Appendix A), is large in the area affected by warm currents (TWC, CWC, and EKWC), accounting for the enhanced LHF (Figs. 5c and 5d) as they transport warm water poleward thereby increasing the saturation specific humidity of the ocean (high q_{sea} compared to q_{air}). In the fall, as both equatorward flowing CCC and poleward flowing CWC weaken in the ECS, and equatorward flowing NKCC develops with offshore meandering of the EKWC (discussed in the next section), the heat loss of the ocean through the LHF is more enhanced at the I-ORS than at the ESROB (Figs. 5e and 5f), which explains the higher magnitude of the fall LHF loss at the I-ORS than at the ESROB (Fig. 3a).

Chapter 4. Discussion

4.1 Meiyu-biau rainband and low SWR in June

Given that the atmospheric response is characterized by an enhanced precipitation over the warm SST of the TWC region in early spring and summer (Xie et al. 2002; Kida et al. 2015; Sasaki and Yamada 2017), it is perhaps of little surprise that the SWR observed only at the I-ORS is low in June. The lowest SWR in June has been observed in the ECS (Hirose et al. 1999; Na et al. 1999; Kim and Chang 2014), which is associated with a large-scale rainband, namely, the meiyu-biau rainband formed by the meiyu-biau front passing from the Tibetan Plateau in the west to Japan in the east along the jet stream (Sampe and Xie 2010; Sasaki et al. 2012; Sasaki and Yamada 2017). Both CFSv2 and MERRA-2 commonly show a decrease in the SWR accompanied by a high (~10 mm day^{-1}) rain rate south of 33°N in June, which is indicative of the broad influence of the meiyu-biau rainband (Figs. 4b and 4e). The strong spatial gradient of the specific humidity owing to the rainband has been suggested by previous studies (Kwon et al. 2005; Tomita et al. 2010; Yim et al. 2015; Sasaki and Yamada 2017). The spatially and temporally reduced June SWRs observed at the I-ORS and reproduced by the two reanalysis products south of 33°N are consistent with the rainband formed by the meiyu-biau front, as previously reported, although the two reanalysis data are not consistent with each other or the observed data in the sense of the absolute SWR (Fig. 4, Tables 3 and 4).

4.2 East Korea Warm Current and high SHF in winter

More heat loss of the ocean through a higher SHF (difference of ~32 W m^{-2}) observed at the ESROB than at the I-ORS in winter is consistent with the results (~40 W m^{-2} in January) reported by Na et al. (1999). Both CFSv2 and MERRA-2 demonstrate such a higher winter SHF in the area of a higher SST along the path of the TWC, CWC, and EKWC, including the ESROB (but excluding the I-ORS) (Figs. 5a, 5b, 6a, and 6b). It is clear that the high winter SHF is derived by the enhanced difference in air–sea temperature $(T_{sea} - T_{air})$ of up to ~10 °C in the area primarily owing to the higher SST, rather than the lower air temperature, which is linked to warm water transported poleward by the TWC, CWC, and EKWC, as suggested by previous studies (Ichikawa and Bearsley 2002; Chang et al. 2004; Yoon and Kim 2009). Note that the isotherms of the air temperature distribute more zonally in contrast to the more meridionally aligned SST isotherms off the east coast of the KP. The results of sensitivity tests support the most significant (65%) role of $(T_{sea} - T_{air})$, as compared to other factors (C_h and U), on the SHF variability (see Appendix A). Thus, a high winter SHF primarily due to $(T_{sea} - T_{air})$ or more likely to the high SST along the paths of the TWC, CWC, and EKWC suggested previously was found from the multi-year observations at the two sites and two reanalysis products described in this study.

4.3 Reversing LHF in spring and fall

The LHFs observed at the ESROB and I-ORS in the spring are inconsistent with the results presented by Na et al. (1999) presumably owing to the lack of observations near the Korean east coast in the previous study. The higher spring LHF loss observed at the ESROB than at the I-ORS, in contrast with the previous results, is also explained by the influence of the TWC, CWC, and EKWC, yielding a large $(q_{sea} - q_{air})$ exceeding 3 g kg^{-1} where the SST is high as the warm water is transported (Figs. 5c, 5d, 6c, and 6d). The value of q_{sea} in spring at the I-ORS, well apart from the paths of the TWC and CWC, is less than 9 g kg^{-1} owing to a lower SST linked to cold water transported equatorward by the weak (not noticeable from the satellite altimetry-derived surface geostrophic current) CCC (Figs. 5c, 5d, 6c, and 6d). Note that q_{air} is aligned more zonally following the air temperature, in contrast with the meridionally shifted q_{sea}, indicating that the influence of these currents along with the results of sensitivity tests (the humidity difference $(q_{sea} - q_{air})$ is the more affecting factor, accounting for 58% of the LHF variations than C_e and U).

In fall, the loss of the ocean's heat through the LHF observed at the I-ORS is higher than that at the ESROB, which is consistent with Na et al. (1999), although the difference reported here is 4–5 times smaller than previously reported (~40-50 W m^{-2} in October). The humidity difference $(q_{sea} - q_{air})$ is significantly (~6 g kg^{-1}) higher in the fall than in the spring at both sites, but more drastically at the I-ORS (Figs. 5e and 5f). At the I-ORS and nearby areas, q_{sea} becomes higher in the fall than in the spring

as the seasonal warming increases the SST and the equatorward flowing CCC weakens. At the ESROB, by contrast, the paths of the poleward flowing TWC separate from the east coast of Korea further south and the equatorward flowing NKCC strengthens, which has a lower q_{sea} in the fall than in the spring (Figs. 6e and 6f). Such seasonal variations of the regional circulation with the surface currents have been previously reported (Chang et al. 2004; Yoon and Kim 2009; Yun et al. 2004; Kim and Min 2008; Lie and Cho 2016; Park et al. 2016), although their impacts on the LHF remain unclear. Although the LHF is primarily determined by $(q_{sea} - q_{air})$ (see Appendix A), U in the fall is doubled at the I-ORS (~8 ms^{-1}) compared with at the ESROB, indicative of the non-negligible role of U on the high LHF at the I-ORS (Oh et al. 2007; Yun et al. 2015). The results on reversing the LHF in the spring and fall primarily owing to the change in regional ocean circulation, presented here, are also consistent with previous suggestions, although not reported.

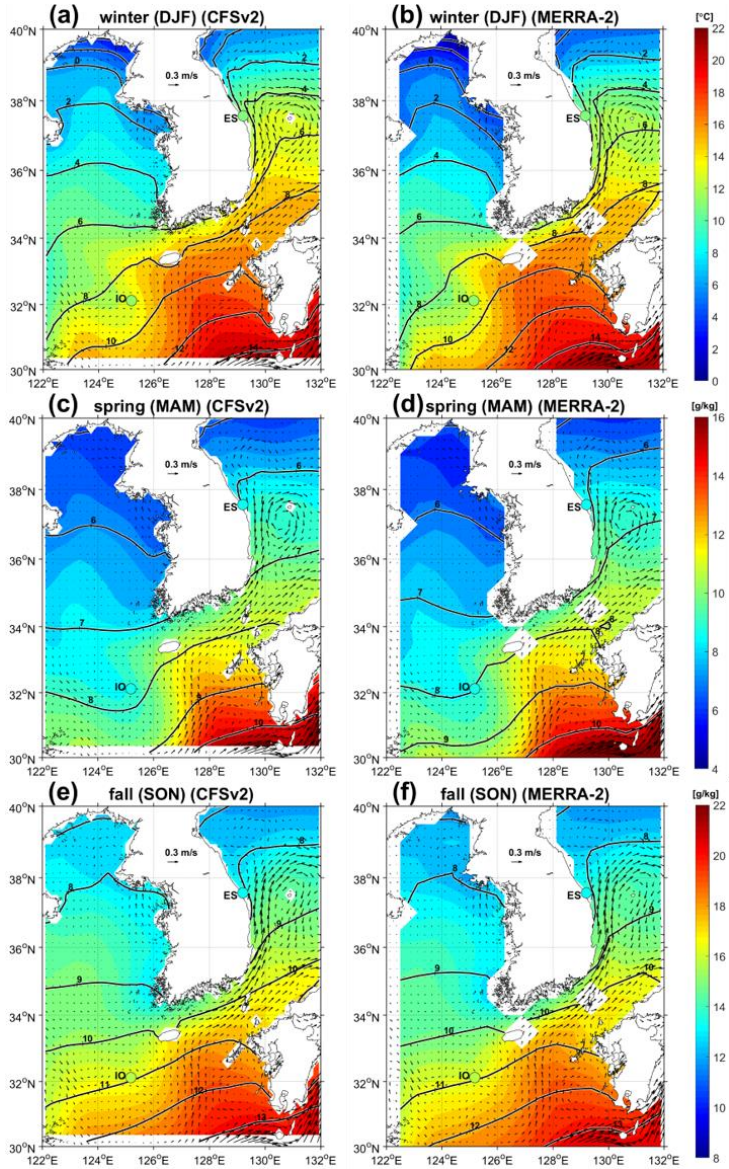

Figure 6. Spatial distribution of (a, b) winter (DJF) SST, (c, d) spring (MAM) saturation specific humidity, and (e, f) fall (SON) saturation specific humidity from (a, c, e) CFSv2 and (b, d, f) MERRA-2 (colors). The 10-m air temperature in ºC and 10-m air specific humidity in g kg^{-1} are shown with contours in (a, b) and (c, d, e, and f), respectively. The surface geostrophic currents for the corresponding seasons are shown with arrows.

Chapter 5. Summary and Conclusion

The seasonal and spatial variations of atmosphere–ocean heat exchange in the seas around the KP were summarized with schematics shown in Fig. 7. In winter and spring, SST at the I-ORS is low owing to the influence of the strengthened CCC as well as wintertime surface cooling, whereas that at the ESROB is high, and is more affected by the EKWC. This results in larger differences in the air–sea temperature and humidity and yields a higher SHF and LHF at the ESROB than at the I-ORS. In fall, in contrast with spring, the SST at the I-ORS is higher than that at the ESROB owing to the weakened CCC with the summer surface warming and offshore meandering of the EKWC with the strengthened NKCC, resulting in larger differences in the air–sea temperature and humidity along with stronger wind, and yielding a higher SHF and LHF at the I-ORS than at the ESROB. In summer, the SWR dominates as the other components of the heat flux are negligible, and the meiyu-baiu rainband distinctly decreases the SWR in the northern ECS (south of 33°N) including the I-ORS (but not at the ESROB) in June.

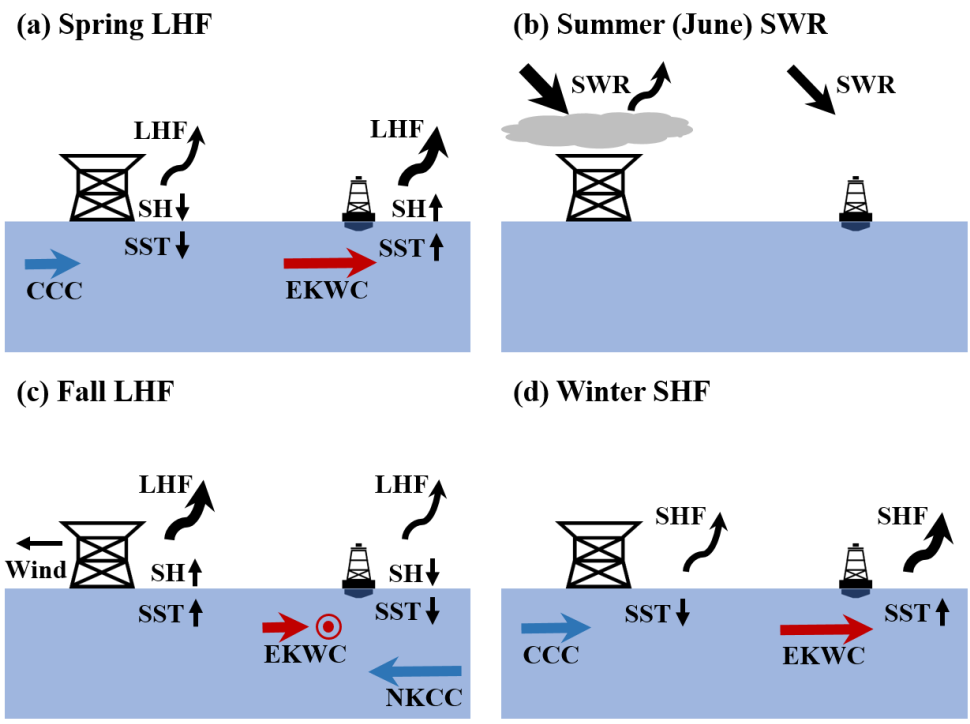

Figure 7. Schematics of the seasonally and spatially varying ocean-atmosphere heat exchange in the seas around the KP including the two observational sites of the I-ORS (marine platform on the left) and the ESROB (surface buoy on the right) for (a) spring (MAM), (b) summer (June), (c) fall (SON), and (d) winter (DJF). Here, SST and SH indicate the sea surface temperature and saturation specific humidity; in addition, regional ocean circulation with warm (red) and cold (blue) currents is shown with arrows (left, south; right, north) and symbol (seaward meandering of EKWC separate from the coast further south in fall).

The differences in the ocean–atmosphere heat exchanges between the two observational sites of the I-ORS and ESROB, located within the vicinity of the fronts between the TWC/CWC and the CCC and between the EKWC and the NKCC, are largely affected by the SST, which is imposed primarily owing to the seasonal change in the regional ocean circulation, rather than atmospheric change. Thus, continuous monitoring of the SST and regional ocean circulation, in addition to marine meteorology, is particularly important for a better understanding of the process and predicting the weather and climate systems through the surface heat flux in the seas around the KP.

Appendix

According to Eq. (1c)–(1d), SHF (LHF) is a function of C_h (C_e), $T_{sea} - T_{air}$ ($q_{sea} - q_{air}$), and U. The remaining variables, ρ and L_e, are treated as constants, e.g., the mean time during the period was used. To see whether the surface heat flux fluctuates to the greatest extent based on any of the variables, a sensitivity test was conducted using data collected at the I-ORS and ESROB. The tests were applied for ranges of variables of up to three standard deviations from the mean with an interval of 1/100 of the range. The Monte Carlo (MC) and Latin-Hypercube One factor At a Time (LH-OAT) methods (Razavi et al. 2015) were applied to the same variables, namely, C_h (C_e), $T_{sea} - T_{air}$ ($q_{sea} - q_{air}$), and U for the input variables and SHF (LHF) for the output variables. The linear regression coefficients between the normalized input variables and the output variable were calculated, from which the new outputs for the entire input data were estimated. Tens of thousands of input sets were randomly generated based on the empirical cumulative density function in the MC method and the interval (1/10,000 of the input value ranges) in the LH-OAT method. For each method, how much the outputs change sensitively according to the randomly made input datasets was calculated. Both methods were conducted ten times for the SHF and LHF for each observational site.

The results of the sensitivity of the SHF and LHF at the two sites to C_h, C_e, $(T_{sea} - T_{air})$, $(q_{sea} - q_{air})$, and U are shown in Fig. A.1. The SHF is the most sensitive to $(T_{sea} - T_{air})$ (65 %), yielding an SHF ranging

from −100 (−130) to +75 (+95) W m^{-2} for the ranges of $(T_{sea} - T_{air})$ at the I-ORS (ESROB), and from −25 (−50) W m^{-2} to zero (zero) for the ranges of both U and C_h. The LHF at the I-ORS is sensitive to $(q_{sea} - q_{air})$ (58 %) and U (29 %), yielding an LHF ranging from −130 W m^{-2} to zero by U and C_e, and from −250 to +140 W m^{-2} by $(q_{sea} - q_{air})$. At the ESROB, the LHF changed by U (C_e) ranges from −230 (−180) W m^{-2} to zero (zero), whereas that by $(q_{sea} - q_{air})$ ranges from −240 to +70 W m^{-2}. The SHF and LHF are concluded to be most sensitive to $(T_{sea} - T_{air})$ and $(q_{sea} - q_{air})$, respectively.

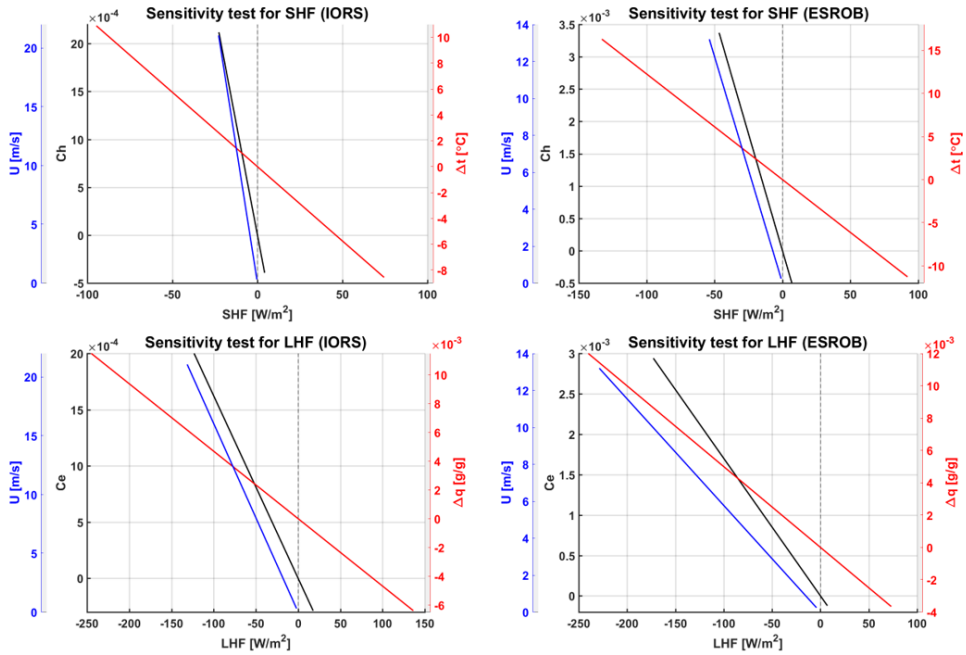

Figure A.1. Results of the sensitivity tests for (up) SHF and (down) LHF at (left) I-ORS and (right) ESROB. The sensitivity of SHF to $(T_{sea} - T_{air})$ (red), C_h (black), and U (blue) versus that of LHF to $(q_{sea} - q_{air})$ (red), C_e (black), and U (blue).

References

Chang, K. I., Teague, W. J., Lyu, S. J., Perkins, H. T., Lee, D. K., Watts, D. R., Kim, Y. B., Mitchell, D. A., Lee, C. M., Kim, K, 2004. Circulation and currents in the southwestern East/Japan Sea: Overview and review. Progress in Oceanography, 61(2-4), 105-156.

Chu, P., Chen, Y., Kuninaka, A., 2005. Seasonal variability of the Yellow Sea/East China Sea surface fluxes and thermohaline structure. Advances in Atmospheric Sciences, 22(1), 1-20.

Fairall, C. W., Bradley, E. F., Rogers, D. P., Edson, J. B., Young, G. S., 1996a. Bulk parameterization of air-sea fluxes for tropical ocean-global atmosphere coupled-ocean atmosphere response experiment. Journal of Geophysical Research: Oceans, 101(C2), 3747-3764.

Fairall, C. W., Bradley, E. F., Godfrey, J. S., Wick, G. A., Edson, J. B., Young, G. S., 1996b. Cool-skin and warm-layer effects on sea surface temperature. Journal of Geophysical Research: Oceans, 101(C1), 1295-1308.

Fairall, C. W., Bradley, E. F., Hare, J. E., Grachev, A. A., Edson, J. B., 2003. Bulk parameterization of air-sea fluxes: Updates and verification for the COARE algorithm. Journal of Climate, 16(4), 571-591.

Gelaro, R., McCarty, W., Suarez, M. J., Todling, R., Molod, A., Takacs, L., Randles, C. A., Darmenov, A., Bosilovich, M. G., Reichle, R., Wargan, K., Coy, L., Cullather, R., Draper, C., Akella, S., Buchard, V., Conaty, A., Silva, A. M. D., Gu, W., Kim, G. K., Koster, R., Lucchesi, R., Merkova, D., Nielsen, J. E., Partyka, G., Pawson, S., Putman, W., Rienecker, M., Schubert, S. D., Sienkiewicz, M., Zhao, B., 2017. The modern-era retrospective analysis for research and applications, version 2 (MERRA-2). Journal of Climate, 30(14), 5419-5454.

Hirose, N., Kim, C. H., Yoon, J. H., 1996. Heat budget in the Japan Sea. Journal of Oceanography, 52(5), 553-574.

Hirose, N., Lee, H. C., Yoon, J. H., 1999. Surface heat flux in the East China Sea and the Yellow Sea. Journal of Physical Oceanography, 29(3), 401-417.

Ichikawa, H., Beardsley, R. C., 2002. The current system in the Yellow and East China Seas. Journal of Oceanography, 58(1), 77-92.

Jin, X., Yu, L., 2013. Assessing high-resolution analysis of surface heat fluxes in the Gulf Stream region. Journal of Geophysical Research: Oceans, 118(10), 5353-5375.

Kawai, Y., Wada, A., 2007. Diurnal sea surface temperature variation and its impact on the atmosphere and ocean: A review. Journal of Oceanography, 63(5), 721-744.

Kida, S., Mitsudera, H., Aoki, S., Guo, X., Ito, S. I., Kobashi, F., Komori, N., Kubokawa, A., Miyama, T., Morie, R., Nakamura, H., Nakamura, T., Nakano, H., Nishigaki, H., Nonaka, M., Sasaki, H., Sasaki, Y. N., Suga, T., Sugimoto, S., Taguchi, B., Takaya, K., Tozuka, T., Tsujino, H., Usui, N., 2015. Oceanic fronts and jets around Japan: a review. Journal of Oceanography, 71(5), 469-497.

Kim, S. B., Chang, K. I., 2014. Calculation of surface heat flux in the Southeastern Yellow Sea using ocean buoy data. The Sea, 19(3), 169-179 (in Korean with English abstract).

Kim, Y. S., Kwon, B. H., 2003. Variations of heat fluxes over the East China Sea and the southern part of the east sea based on the buoy data. Asia-Pacific Journal of Atmospheric Sciences, 39(3), 337-345.

Kim, Y. H., Min, H. S., 2008. Seasonal and interannual variability of the North Korean Cold Current in the East Sea reanalysis data. Ocean and Polar Research, 30(1), 21-31 (in Korean with English abstract).

Kim, H., Kim, C. H., Shin, H. R., 2016. Analysis of sea surface temperature simulation in the Northwestern Pacific and the East Asian Marginal Seas using HadGEM2-AO. Ocean and Polar Research, 38(2), 89-102 (in Korean with English abstract).

Kwak, H., Cho, Y. K., Seo, G. H., Tak, Y. J., Park, H. S., You, S. H., Seo, J. W., 2015. Seasonal sea surface temperature asymmetry in the Northwestern Pacific Marginal Seas. Terrestrial, Atmospheric & Oceanic Sciences, 26(3).

Kwon, M., Jhun, J. G., Wang, B., An, S. I., Kug, J. S., 2005. Decadal change in relationship between east Asian and WNP summer monsoons. Geophysical research letters, 32(16).

Lee, S. H., Zo, I. S., Lee, K. T., Kim, B. Y., Jung, H. S., Rim, S. H., Byun, D. S., Lee, J. Y., 2017. A strategy for environmental improvement and internationalization of the IEODO ocean research station's radiation observatory. The Sea, 22(3), 118-134 (in Korean with English abstract).

Lie, H. J., Cho, C. H., 2016. Seasonal circulation patterns of the Yellow and East China Seas derived from satellite-tracked drifter trajectories and hydrographic observations. Progress in Oceanography, 146, 121-141.

Liu, N., Wu, D., Lin, X., Meng, Q., 2014. Seasonal variations of air-sea heat fluxes and sea surface temperature in the northwestern Pacific marginal seas. Acta Oceanologica Sinica, 33(3), 101-110.

Murphy, D. M., Koop, T., 2005. Review of the vapour pressures of ice and supercooled water for atmospheric applications. Quarterly Journal of the Royal Meteorological Society: A Journal of the Atmospheric Sciences, Applied Meteorology and Physical Oceanography, 131(608), 1539-1565.

Na, J., Seo, J., Lie, H. J., 1999. Annual and seasonal variations of the sea surface heat fluxes in the East Asian marginal seas. Journal of Oceanography, 55(2), 257-270.

Nam, S. H., Kim, G., Kim, K. R., Kim, K., Cheng, L. O., Kim, K. W., Ossi, H., Kim, Y. G., 2005. Application of real-time monitoring buoy systems for physical and biogeochemical parameters in the coastal ocean around the Korean peninsula. Marine Technology Society Journal, 39(2), 70-80.

Oh, H. M., Ha, K. J., Shim, J. S., Hyun, Y. K., Yun, K. S., 2007. Seasonal characteristics of turbulent fluxes observed at leodo Ocean Research Station. Atmosphere, 17(4), 421-433 (in Korean with English abstract).

Park, M. J., Kim, Y. S., Kwon, B. H., Han, Y. H., 2003. Characteristics of heat flux and turbulent kinetic energy over the Yellow Sea and the South Sea. Korean Journal of the Atmospheric Sciences, 6(1), 1-11.

Park, K. A., Park, J. E., Choi, B. J., Byun, D. S., Lee, E. I., 2013. An oceanic current map of the East Sea for science textbooks based on scientific knowledge acquired from oceanic measurements. The Sea, 18(4), 234-265 (in Korean with English abstract).

Park, J. H., Chang, K. I., Nam, S. H., 2016. Summertime coastal current reversal opposing offshore forcing and local wind near the middle east coast of Korea: Observation and dynamics. Geophysical Research Letters, 43(13), 7097-7105.

Park, J. H., Lee, S. W., Lee, S. U., Gil, K. N., Nam, S. H., 2018. A system for real-time and continuous monitoring of environmental information to prevent disasters off the east coast of Korea and its application to Typhoon Sanba (2012) case. Journal of Coastal Disaster Prevention, 5(3), 135-142 (in Korean with English abstract).

Razavi, S., Gipta, H. V., 2015. What do we mean by sensitivity analysis? The need for comprehensive characterization of “global” sensitivity in Earth and Environmental systems models. Water Resources Research, 51(5), 3070-3092.

Saha, S., Moorthi, S., Wu, X., Wang, J., Nadiga, S., Tripp, P., Behringer, D., Hou, Y. T., Chuang, H. Y., Iredell, M., Ek, M., Meng, J., Yang, R., Mendez, M. P., Dool, H. V. D., Zhang, Q., Wang, W., Chen, M., Becker, E., 2014. The NCEP climate forecast system version 2. Journal of Climate, 27(6), 2185-2208.

Sampe, T., Xie, S. P., 2010. Large-scale dynamics of the meiyu-baiu rainband: Environmental forcing by the westerly jet. Journal of Climate, 23(1), 113-134.

Sasaki, Y. N., Yamada, Y., 2017. Atmospheric response to interannual variability of sea surface temperature front in the East China Sea in early summer. Climate Dynamics, 51(7-8), 2509-2522.

Sasaki, Y. N., Minobe, S., Asai, T., Inatsu, M., 2012. Influence of the Kuroshio in the East China Sea on the early summer (Baiu) rain. Journal of Climate, 25(19), 6627-6645.

Seo, G. H., Cho, Y. K., Choi, B. J., Kim, K. Y., Kim, B. G., Tak, Y. J., 2014. Climate change projection in the Northwest Pacific marginal seas through dynamic downscaling. Journal of Geophysical Research: Oceans, 119(6), 3497-3516.

Shim, J. S., Chun, I. S., Min, I. K., 2004. Construction of Ieodo Ocean Research Station and its operation. Proceedings of the 14th international offshore and polar engineering conference, Toulon, France, 351-357.

Sim, J. E., Shin, H. R., Hirose, N., 2018. Comparative analysis of surface heat fluxes in the East Asian marginal seas and its acquired combination data. Journal of Korean Earth Science Society, 39(1), 1-22.

Small, R. D., deSzoeke, S. P., Xie, S. P., O'Neill, L., Seo, H., Song, Q., Cornillon, P., Spall, M., Minobe, S., 2008. Air-sea interaction over ocean fronts and eddies. Dynamics of Atmospheres and Oceans, 45(3-4), 274-319.

Smith, S. D., Fairall, C. W., Geernaert, G. L., Hasse, L., 1996. Air-sea fluxes: 25 years of progress. Boundary-Layer Meteorology, 78(3-4), 247-290.

Subrahamanyam, D. B., Ramachandran, R., Rani, S. I., Kumar, B. P., 2007. Air-sea interaction processes over the East-Asian marginal seas surrounding the Korean peninsula. Annales Geophysicae, 25(7), 1477-1486.

Tomita, T., Nonaka, M., Yamaura, T., 2010. Interannual variability in the subseasonal northward excursion of the Baiu front. International Journal of Climatology, 30(14), 2205-2216.

Ward, B., 2006. Near-surface ocean temperature. Journal of Geophysical Research: Oceans, 111(C2).

Webster, P. J., Lukas, R., 1992. TOGA COARE: The coupled ocean-atmosphere response experiment. Bulletin of the American Meteorological Society, 73(9), 1377-1416.

Xie, S. P., Hafner, J., Tanimoto, Y., Liu, W. T., Tokinaga, H., Xu, H., 2002. Bathymetric effect on the winter sea surface temperature and climate of the Yellow and East China Seas. Geophysical Research Letters, 29(24), 81-1.

Yim, S. Y., Wang, B., Xing, W., Lu, M. M., 2015. Prediction of Meiyu rainfall in Taiwan by multi-lead physical–empirical models. Climate Dynamics, 44(11-12), 3033-3042.

Yoon, J. H., Kim, Y. J., 2009. Review on the seasonal variation of the surface circulation in the Japan/East Sea. Journal of Marine Systems, 78(2), 226-236.

Yu, L., Weller, R. A., 2007. Objectively analyzed air-sea heat fluxes for the global ice-free oceans (1981-2005). Bulletin of the American Meteorological Society, 88(4), 527-540.

Yun, J. Y., Magaard, L., Kim, K., Shin, C. W., Kim, C., Byun, S. K., 2004. Spatial and temporal variability of the North Korean Cold Water leading to the near-bottom cold water intrusion in Korea Strait. Progress in Oceanography, 60(1), 99-131.

Yun, J., Oh, H., Ha, K. J., 2015. Observation and analysis of turbulent fluxes observed at Ieodo Ocean Research Station in autumn 2014. Atmosphere, 25(4), 707-718 (in Korean with English abstract).

국문 초록

2011–2016년 한반도 주변 해역에서 해양–대기 열 교환의 계절적 및 공간적 변동

여 다 은
지구환경과학부
서울대학교 대학원

해양–대기 열 교환은 전지구적 기후 및 기상 시스템에 영향을 끼치기 때문에 이를 이해하고 그 변동 특성을 파악하는 것이 매우 중요하다. 한반도 주변 해역에서 동아시아 몬순과 관련된 대부분의 해양 및 대기 변수의 연변동은 잘 알려져 있는 반면 해양–대기 열 교환의 연변동은 관측 자료의 부족으로 여전히 잘 알려져 있지 않다. 특히, 대마난류의 영향을 받는 한반도 주변 해역에서는 겨울 몬순(북서풍) 동안 상대적으로 따뜻한 해양 위에 차갑고 건조한 대기가 위치하면서 해양–대기 열 교환이 증가하는데, 이는 재분석장 자료에서 종종 과대 또는 과소 추정된다. 본 연구에서는 2011–2016년 기간 동안 이어도 해양과학기지(이하 이어도 기지)와 동해 실시간 관측 부이(이하 동해 부이)의 관측 자료와 재분석장 자료(CFSv2와 MERRA–2)로부터 해양–대기 열속의 평균 연변동을 추정했다. 동해 연안에 위치한 동해 부이에서의 순열속(–68 W m^{-2}, 양수 값이 대기에서 해양으로의 열 이동을 의미)은 한반도 남서쪽 약 250 km에 위치한 이어도 기지에서의 순열속(+78 W m^{-2})보다 146 W m^{-2}만큼 더 크게 나타났으나, 예외적으로 6월에는 이어도 기지에서 Meiyu–Baiu rainband로 인해 단파복사가 208 W m^{-2}만큼 감소하여 순열속 차이가 줄어든다. 이어도 기지에 비해 동해 부이에서 겨울철

과 봄철은 각각 더 많은 현열속(32 W m^{-2})과 잠열속(47 W m^{-2}) 손실, 가을철은 더 적은 잠열속(22 W m^{-2}) 손실이 나타난다. CFSv2는 이어도 기지 (동해 부이)에서 평균 순열속, 겨울철 현열속, 봄철과 가을철 잠열속을 -24, −84 -41, −180 W m^{-2} (−43, −110, −56, −120 W m^{-2})으로 재현하고, MERRA−2는 -28, −56, −26, −161 W m^{-2} (−108, −134, −71, −155 W m^{-2})으로 재현한다. 관측 자료와의 편이(bias) 오차에도 불구하고 두 재분석장 자료의 현열속과 잠열속 공간 분포는 이 해역에서 해양−대기 열 교환의 연변동에 대한 해류의 유의미한 영향을 보여준다.

주요어 : 이어도 해양과학기지, 동해 실시간 해양 부이, 해양−대기 열 교환, 계절 변동, 대마난류, 제주난류, 중국연안류, 동한난류, 북한한류
학 번 : 2017−29237